

Low-Luminosity AGNs at the Highest Resolution: Jets or Accretion Flows?

James M. Anderson^{1,2}

janderso@nrao.edu

James S. Ulvestad¹

julvesta@nrao.edu

and

Luis C. Ho³

lho@ociw.edu

ABSTRACT

Six low-luminosity active galactic nuclei have been imaged at multiple frequencies from 1.7–43 GHz (2.3–15 GHz for three of the galaxies) using the Very Long Baseline Array. In spite of dynamic ranges of about 100 in several frequency bands, all six galaxies remain unresolved, with size limits at 8.4 GHz of 10^3 – 10^4 times the Schwarzschild radii of the black holes inferred at their galactic centers. The galaxy spectra are roughly flat from 1.7 to 43 GHz, rather than steepening to classical optically thin synchrotron spectra at high frequencies. Although the spectral slopes somewhat resemble predictions for advection-dominated accretion flows, the luminosities are too high for the black hole masses of the galaxies and the slight spectral steepening at high frequencies cannot be explained by standard simple models of such accretion flows. In contrast, compact jets can accommodate the average spectral index, the relatively high radio luminosity, and the unresolved appearance, but only if the jets in all six galaxies are fairly close to our line of sight. This constraint is in agreement with inclination angle predictions for five of the six AGNs based on the dusty torus unification model.

¹National Radio Astronomy Observatory, P.O. Box O, 1003 Lopezville Road, Socorro, NM 87801.

²Department of Physics, New Mexico Institute of Mining and Technology, Socorro, NM 87801.

³The Observatories of the Carnegie Institution of Washington, 813 Santa Barbara Street, Pasadena, CA 91101.

Subject headings: galaxies: active — galaxies: nuclei — galaxies: Seyfert — radio continuum: galaxies

1. Introduction

The physical processes that control the accretion and outflow in low-luminosity active galactic nuclei (LLAGNs) are still not well understood. In their study of the Palomar Seyfert sample, Ho, Filippenko, & Sargent (1997a) found that almost 40% of bright ($B_T < 12.5$ mag) nearby galaxies have optical spectra indicating the presence of an AGN. Although their line emission resembles scaled down versions of more luminous Seyfert nuclei, which are thought to be driven by accretion in thin disks, LLAGN properties at other wavelengths suggest that different processes are at work. Whereas “classical” Seyfert galaxies have radio spectral indices $\alpha \approx -0.7$, where $S_\nu \propto \nu^{+\alpha}$, almost half of the low-luminosity Seyfert galaxies in the Palomar Seyfert sample have flat or positive spectral indices (Ulvestad & Wilson 1989; Ho & Ulvestad 2001, hereafter HU01; Ulvestad & Ho 2001a, hereafter UH01a). Similar results have been found for low-ionization nuclear emission regions (LINERs) and other AGNs in the Palomar sample (Nagar et al. 2000, 2002; Filho, Barthel, & Ho 2000, 2002). These flat-spectrum objects typically appear compact on arcsecond scales, and high resolution studies with the Very Long Baseline Array⁴ (VLBA; Napier et al. 1993) show that they remain compact even on milliarcsecond scales (Falcke et al. 2000; Ulvestad & Ho 2001b, hereafter UH01b).

Following the work of Ferrarese & Merritt (2000), Gebhardt et al. (2000), and others, it has become clear that both normal and active galaxies with bulges have supermassive black holes at their nuclear centers. Accretion onto these black holes is thought to fuel the AGN process for both “normal” and low-luminosity AGNs. Since their black hole masses cover roughly the same range (see, for example, Ho 2002), the mass of the central object cannot account for the difference in emission levels. The explanation for why LLAGNs emit so little radiation may be either that they have far less mass accreting onto them, or that the dominant mode of the accretion mechanism itself must be different, or both.

The center of our own Milky Way Galaxy has been used as the testbed for many models that attempt to explain the physics of LLAGNs. Acceleration measurements of stellar orbits near the source Sagittarius A* (Sgr A*) leave little doubt as to the existence of a supermassive black hole of $\sim 3.3 \times 10^6 M_\odot$ at the Galactic Center (Ghez et al. 2003; Schödel et al. 2003).

⁴The VLBA is operated by the National Radio Astronomy Observatory, a facility of the National Science Foundation, operated under cooperative agreement by Associated Universities, Inc.

Invisible in the optical and near-infrared, Sgr A* has a mildly inverted spectrum from 1 to 100 GHz (Falcke et al. 1998). The luminosity of Sgr A* is extremely low, even compared with other LLAGNs. Advection dominated accretion flows (ADAFs) have been used to explain the spectral energy distributions (SEDs) of Sgr A* and other LLAGNs during the past decade (Narayan & Yi 1994, 1995; Narayan, Yi, & Mahadevan 1995; Narayan, Mahadevan, & Quataert 1998b). In the ADAF model, a hot plasma develops in which the protons decouple from the electrons, allowing the protons to carry most of the energy released by the accretion process into the black hole, limiting the amount that is radiated away. Hot thermal electrons generate synchrotron radiation that is self-absorbed, resulting in a radio spectral index of ~ 0.4 (Mahadevan 1997). Bremsstrahlung and inverse-Compton processes generate additional emission, producing a relatively well-defined spectrum from radio through X-ray frequencies.

An alternative hypothesis for the emission from LLAGNs is the compact-jet model (Falcke & Biermann 1995; Falcke 1996; Falcke & Biermann 1999; Falcke & Markoff 2000). Plasma is ejected in a collimated beam away from the black hole, and expands sideways to form a cone-shaped emission region. Synchrotron emission is initially self-absorbed, becoming progressively more transparent to lower frequencies as the material travels away from the black hole, producing an overall radio spectrum that can be quite flat.

With both ADAF (and other related low-radiation accretion flows) and jet models failing to account for the overall SEDs in LLAGNs (see, for example, Narayan et al. 1998b; Yuan, Markoff, & Falcke 2002a), several attempts have been made recently to combine the two models. Yuan et al. (2002a) have reasonable success in explaining the spectrum of Sgr A* with this combined model. Although this work has been extended to NGC 4258 (Yuan et al. 2002b), rigorous testing of a large sample of LLAGNs in the nearby universe has yet to be performed. These LLAGNs are many orders of magnitude *more* luminous than Sgr A*, but are also several orders of magnitude *less* luminous than “classical” AGNs. They therefore occupy a luminosity range that has thus far had few detailed studies.

We have formed an LLAGN sample from the HU01 study, selecting objects which have 5 GHz Very Large Array (VLA) peak flux densities between 5 and 30 mJy and spectral indices at milliarcsecond resolution of $\alpha_{1.4}^5 > -0.35$. In this paper we discuss simultaneous, multifrequency radio imaging of six LLAGNs. The purpose of these observations, and the point of the present paper, is to measure the sizes and radio spectra of LLAGNs within 10^4 Schwarzschild radii of their black holes, and to determine what constraints these parameters can place on possible ADAF and jet models.

2. Observations and Analysis

NGC 3147, NGC 4203, and NGC 4579 were previously observed with the VLBA at 1.7–8.4 GHz (UH01b). Here we present new VLBA observations of these galaxies at 8.4–43 GHz and 2.3–15 GHz observations of NGC 4168, NGC 4235, and NGC 4450, which have no previous VLBA observations. Details of the observations are presented in Table 1. Each galaxy was observed in a single 10 hour run at a data recording speed of 256 Mb s^{-1} , with individual frequencies observed multiple times in short time blocks spread throughout the full 10 hours to improve (u, v) coverage. The interleaving of observing frequencies also results in a mean observing epoch which is nearly simultaneous for all frequencies; this is important in order to properly measure the spectral index, as LLAGNs are known to have variable radio emission (e.g., Nagar et al. 2002). We applied an amplitude calibration using a priori gain values together with system temperatures measured during the observations; typically, this calibration is accurate to within 5% at the lower frequencies and 10% for 22 and 43 GHz.

Initial clock and atmospheric (phase) errors were derived from the calibrator sources listed in Table 1 using the technique of phase-referencing (Beasley & Conway 1995)⁵. This initial calibration was used to determine the galaxy core positions shown in Table 2. Uncertainties in the positions generally are dominated by the uncertainties in the phase calibrator positions, but contributions from ionospheric and tropospheric phase fluctuations and residual phase errors can be important for some objects.

Each galaxy was detected at all frequencies in this initial imaging process. Phase-only self-calibration was then applied iteratively. The resulting rms noise levels in the images far away from the galaxy cores are consistent with predictions and vary from $40\text{--}70 \mu\text{Jy beam}^{-1}$ for 2.3–8.4 GHz, up to about $500 \mu\text{Jy beam}^{-1}$ at 43 GHz. Beam widths range from $\sim 6 \text{ mas}$ at 2.3 GHz, to $\sim 1.6 \text{ mas}$ at 8.4 GHz, to $\sim 0.4 \text{ mas}$ at 43 GHz using natural weighting.

Similar processing steps were performed on the substantially brighter check sources, showing that all of the significant phase variations were corrected in the target self-calibration procedures, except the 43 GHz observations of NGC 3147 and NGC 4203, for which self-calibration failed. Therefore, the 43 GHz flux densities for NGC 3147 and NGC 4203 have been scaled from the initial phase-referenced values by the fractional increase in coherence seen in the check sources and assigned a large uncertainty for potential differences between the target and check source decoherence.

⁵The phase referencing involves repetitive switching between a strong calibrator source and the target galaxy in order to calibrate the atmospheric phase for the galaxy. Our switching cycle ranged from 4 minutes at the lower frequencies to 45 seconds at the higher frequencies. Another bright, nearby check source is occasionally observed to test the effectiveness of the phase calibration.

The integrated flux densities for the target galaxies as estimated by Gaussian fitting are shown in Table 3. Since we have only one overlapping frequency between UH01b and our higher frequency observations, we correct for possible variability by shifting the low-frequency data for NGC 3147, NGC 4203, and NGC 4579, so that the 8.4 GHz flux densities are identical at the two epochs and the spectra between .14 and 8.4 GHz are unchanged. This amounts to an overall shift in luminosity, with a maximum change of 19% for NGC 4579. Estimated uncertainties from self-calibration and measurement errors have been added in quadrature to the overall uncertainties in the amplitude scale, in order to derive the final flux-density uncertainties. The LLAGN cores for these objects contain virtually all of the flux seen on larger angular size scales with the VLA (UH01b; J. M. Anderson, et al., in preparation), indicating that there is no significant emission from large-scale features such as parsec-scale jets.

3. Results

3.1. LLAGN Radio Images

Our deep observations have resulted in images with signal-to-noise levels of ~ 100 for frequencies of 2.3–15 GHz. No significant features reminiscent of jets were seen well above the noise level in any of the six LLAGNs in this study. NGC 4579, the brightest object with the correspondingly highest signal-to-noise levels, has an extension to the northeast visible at both 8.4 and 15 GHz, but this is only seen at the 2σ level and represents less than 1% of the total flux in the image. Figure 1 presents 8.4 GHz images of our LLAGNs; images at other wavelengths are similarly pointlike.

Gaussian component fitting with the AIPS task JMFIT confirms the visual impression that all of the VLBA images are dominated by a single unresolved component. Table 4 shows 3σ upper limits to the major axes of the component sizes at 8.4 GHz in addition to the beam sizes. The VLBA size upper limits restrict the physics of the emission regions for these LLAGNs. Table 4 shows the resulting lower limits to the brightness temperatures and upper limits to the *radius* of the emission region (in Schwarzschild radii, R_S).

3.2. LLAGN Core Shift

The process of phase referencing not only allows weak sources to be observed with VLBI techniques, it also allows the measurement of accurate positions relative to the phase reference source. This process can, in theory, allow the detection of a core position shift

as a function of frequency. Such a core shift is one of the predictions of the compact-jet models (Falcke & Biermann 1999). Our measurements have sufficient signal-to-noise to permit measurement of the core positions to $\ll 0.1$ mas. Unfortunately, any core shift within the phase calibrator, and, more importantly, phase fluctuations due to the ionosphere and the troposphere can affect measurements to detect core shift. The measured core shifts prior to self-calibration for our target and check sources are 0.2–0.5 mas between 8.4 and 15 GHz, extending to several milliarcseconds between 2.3 and 15 GHz along roughly straight directions as the frequency is decreased. The angular size of the shift is roughly proportional to the square of the wavelength, suggesting that the measured core shifts are due to residual phase delays in the ionosphere (see Figure 2). Models of the electron content of the ionosphere for each observation were obtained from cddisa.gsfc.nasa.gov (Walker & Chatterjee 1999); these models predict ionosphere-induced position shifts between the phase calibrators and other sources ranging from 0.2 to 0.5 mas between 8.4 and 15 GHz, roughly in agreement with our measurements. The directions of the core shifts for the target and check source pairs are also consistent with residual ionospheric delays. We are therefore left with an upper limit to any intrinsic core shift of ~ 0.3 mas between 8.4 and 15 GHz.

3.3. LLAGN Radio Spectra

Figure 3 shows the radio spectra for the six LLAGNs in this paper. The spectra are extremely flat. In general, the spectra rise slightly up to about 5–10 GHz then become flat or even turn over slightly. The 2.3–5.0 GHz spectral indices ($\alpha_{2.3}^{5.0}$) are remarkably uniform (see Table 5); the 8.4–15 GHz spectral indices ($\alpha_{8.4}^{15}$) also are similar to one another, although there are two outliers. The high frequency data at 22 and 43 GHz, although a bit noisy, indicate that the SEDs continue to be flat at high frequencies.

The similarity among the spectra suggests that the physical mechanism responsible for the radio emission is the same in all six objects. The radio powers are all within a factor of 200 of one another, and the inferred black hole masses are also within a factor of 20 of one another (see Table 2), with the more massive objects having higher radio powers, so the general physical conditions in these six objects would appear to be very similar. We have combined the individual spectra to make the mean SEDs shown in Figure 4. After normalizing each galaxy spectrum to unity at either 2.3 or 8.4 GHz, an unweighted mean was calculated for each frequency, as well as the rms scatter about the mean. The statistical uncertainties in the mean values are about 10% for all points in the curve normalized at 8.4 GHz.

The galaxy spectra are all very similar at low frequencies, as indicated by the small

error bars at 1.7 and 5.0 GHz in the curve normalized at 2.3 GHz in Figure 4. In contrast, the behavior around 5 to 8 GHz is more varied, with some spectra continuing to rise while others actually fall. Then, around 15 GHz the spectra become more similar to one another again as most of the spectra become relatively flat. The data suggest a phenomenon where the spectra turn from slightly rising to being flat, with the turnover frequency varying from one galaxy to the next.

The low-frequency portion of the mean spectrum rises modestly with $\alpha_{1.7}^{8.4} = 0.16 \pm 0.08$ in the data normalized at 8.4 GHz. The spectrum then turns over slightly (but is also consistent with being completely flat) with $\alpha_{8.4}^{22} = -0.11 \pm 0.13$. The overall spectrum is quite smooth — a least squares fit for a constant spectral index from 1.7 to 43 GHz gives $\bar{\alpha} = 0.084 \pm 0.029$ with an rms scatter of only 7%.

4. Comparison with the ADAF Model

Although ADAF models have had some success in explaining the infrared through X-ray behavior of black hole systems, the standard ADAF models have traditionally been less than satisfactory at explaining the relatively strong radio emission as compared with the submillimeter and X-ray emission (e.g., Manmoto, Mineshige, & Kusunose 1997; Narayan et al. 1998a,b). ADAF models have become less popular over the past few years, mostly because they are unstable to convection and mass loss in winds, as pointed out in the early paper by Narayan & Yi (1994). Modifications to ADAFs, such as the introduction of a nonthermal electron distribution (e.g., Yuan, Quataert, & Narayan 2003) to increase the radio luminosity or the introduction of outflow winds (e.g., Blandford & Begelman 1999) to lower the effective accretion rates, can improve fits to individual objects. However, these models are inevitably more complicated, and we defer comparisons with such models to future publications. Instead, we will concentrate here on the simple ADAF model, which does illustrate the basic features of radiatively inefficient accretion systems, and may play an important role in some portions of the emission spectrum.

In the basic ADAF model (e.g., Narayan & Yi 1995; Narayan et al. 1998b), the accretion disk surrounding the black hole is geometrically thick, with the height of the disk on the order of the radius from the black hole. Synchrotron emission, radiated from thermal electrons in the accretion disk, is self-absorbed at high frequencies close to the black hole, becoming optically thin to progressively lower frequencies further away from the black hole. For the radio frequencies of interest here, the typical size of the emission region is a few hundred Schwarzschild radii. This is considerably less than the upper limits to the sizes of our LLAGNs shown in Table 4. The distribution of the emission on the sky does depend on the

viewing angle somewhat, but should be quite symmetric about the center of the black hole for our observing frequencies. Therefore, the ADAF model predicts extremely small core shifts with frequency, well within our upper limits.

A proper treatment of the emission spectrum from ADAFs requires a detailed numerical computation. We will present the results of such calculations in a future paper, and for this paper we instead use the scaling laws provided by Mahadevan (1997, hereafter M97). Although various approximations used in the derivation of these scaling laws reduce their accuracy, the luminosity results at high radio frequencies are probably accurate to within a factor of 2 or so for the basic ADAF model. A power per unit frequency interval is given by M97’s equation 25 in terms of the mass of the black hole, the observing frequency, and the mass accretion rate scaled to units of the Eddington accretion rate (\dot{m}). Other “variables” explicit or implicit in this equation can be rewritten in terms of these three parameters (§5 and the Appendices of M97). Figure 5 shows the predicted 43 GHz radio power as a function of accretion rate for the black hole masses of our six LLAGNs. Except for an overall scaling factor, the curves are nearly all the same, as the ADAF radio power dependence on black hole mass and accretion rate is nearly separable. This figure illustrates the important fact that the basic ADAF model predicts a maximum radio power at an accretion rate of about $\dot{m} = 10^{-2.5}$.

This maximum power is less than the observed radio power, as shown in Figure 6, where the maximum possible radio power in the M97 model is shown as a function of frequency together with the observed spectra for NGC 3147, NGC 4203, and NGC 4579 (results for the other three galaxies are qualitatively similar). The ADAF model spectra are generally more than an order of magnitude below the observed spectra. The only exception is NGC 3147, where the model comes within a factor of 2.5 of the data at the highest frequencies. The ADAF spectra have a continuous spectral index of $\alpha = +0.4$, significantly larger than the overall spectral indices of the sample galaxies.⁶ As shown by Table 5, most of the spectral indices at low frequencies are reasonably consistent with the ADAF prediction, but the observed spectra generally turn over slightly at higher frequencies, despite the ADAF model predicting a continuous rise to submillimeter frequencies. Therefore, basic ADAFs probably make no significant contribution to the radio output of our LLAGNs, except possibly in NGC 3147 where the slight rise at high frequencies may or may not be due to an ADAF.

⁶Mahadevan notes that his model prediction for the radio power spectrum does not fully account for the ADAF dependence on radius, and suggests that the actual dependence should be closer to $P_\nu \propto \nu^{1/3}$, which could raise the radio luminosity somewhat. The M97 model also assumes that the ADAF is viewed pole-on. We plan to produce numerical simulations of the ADAF model which account for such dependencies in a future paper.

Modifications to include a population of nonthermal electrons appear necessary to generate the observed radio powers and spectral indices from ADAF-based systems. We believe that such modifications should allow ADAFs to remain a viable model for LLAGN emission.

5. Comparison with the Jet Model

5.1. Model Comparison

UH01b concluded that the most natural way to account for the SEDs of NGC 3147, NGC 4203, and NGC 4579 in the radio and X-ray was to invoke a jet to explain the radio emission in combination with an ADAF to explain the X-ray emission. Compact jet models can easily accommodate the flux densities and spectral indices of our LLAGNs. Inspection of one jet model has interesting implications for the physics of LLAGN accretion regions.

Falcke & Biermann (1999, hereafter FB99) present a set of simplified analytic equations for their jet model of radio emission from black hole accretion systems based on the conical jet model of Blandford & Königl (1979). The model requires information about the inclination of the jet axis to the line of sight (i , with $i = 0^\circ$ having the jet directed toward the observer) and the characteristic angular size of the emission region (Φ_{jet}) in order to calculate the jet power (Q_{jet}) and characteristic electron Lorentz factor (γ_e). Their model gives results consistent with observations for LLAGN systems such as Sgr A* and NGC 4258. They suggest that a typical value of γ_e for LLAGNs may be ~ 300 , and their equation 20 provides a means to calculate the jet power in terms of the radio flux and inclination angle. By additionally using FB99 equations 8 and 16, Φ_{jet} can be calculated as a function of i .

Figure 7a shows the jet model results for the angular size of NGC 4579 using three different values of γ_e . The first model uses FB99 equation 20 with $\gamma_e = 300$ (solid lines). For small inclination angles (jet pointed at the observer) the angular size is small, while for large i the angular size becomes very large. The expected inclination angle for a randomly oriented jet is 60° , which corresponds to $\Phi_{\text{jet}} = 2.0$ mas at 8.4 GHz for NGC 4579. This is much larger than our upper limit from the VLBA imaging of NGC 4579. In order for this jet model to be valid, the 0.54 mas upper limit to the size requires $i \leq 40^\circ$. The second model uses the parameters FB99 derived for NGC 4258, where a jet is seen by the VLBA (e.g. Herrnstein et al. 1998), with $\gamma_e = 630$ (dotted lines). For most inclination angles, Φ_{jet} is much larger in the $\gamma_e = 630$ model compared to the $\gamma_e = 300$ model, and the 0.54 mas upper limit in size further restricts the inclination to $i \leq 27^\circ$. Although decreasing γ_e from the moderate value of 300 does slightly decrease Φ_{jet} at small inclination angles, a singular point in the FB99 equations (resulting from simplifications FB99 made to their formulae) produces

extremely large Q_{jet} values, and hence Φ_{jet} values, at progressively smaller inclination angles as γ_e is reduced. A small decrease to $\gamma_e = 250$ (dashed lines) causes the model to predict infinite size at $i = 56^\circ$. Thus, the $\gamma_e = 300$ model closely represents the least restrictive model on the allowable inclination angle range.

In the FB99 model, “the characteristic size scale of the core region is actually equivalent to the offset of the radio core center from the dynamical center.” For large i , one expects to see both sides of the jet, and Φ_{jet} is then about half of the full extent of the radio emission. However, for small i , Φ_{jet} may not represent the *size* of the emission region, but its position shift from the actual location of the dynamical center (the black hole) as the jet becomes more and more beamed toward the observer. In this case, the correct comparison is the core shift between two frequencies predicted by the jet model. Figure 7b shows the predicted core shift between 8.4 and 15 GHz for NGC 4579. Once again, the predicted shifts are significantly larger than our upper limits for large i , requiring $i \leq 42^\circ$ (30°) for the moderate (NGC 4258) model for our 0.3 mas core-shift upper limit.

Table 4 shows the results for this simple model analysis for our LLAGN sample at 8.4 GHz. The Φ_{jet} values for a jet inclination angle of 60° are *all* larger than our VLBA size upper-limits. Our upper limits to the core size, and our upper limits to any possible core shift constrain the $\gamma_e = 300$ jet models to have $i \lesssim 50^\circ$ for all of our galaxies. Jet models with larger γ_e require even smaller inclination angles, and jet models with smaller γ_e are not viable for large inclination angles. Essentially, there is no viable range of parameter space which allows large-inclination angle jets in the FB99 model. Improvements to the analytic simplifications at low γ_e values *may* allow the jets to be smaller than our upper limits, but the required jet power would then be excessively large. One possible way to decrease the jet size while maintaining the basic Blandford & Königl (1979) conical jet structure would be to allow the energy density in ions to be much greater than the energy density in electrons ($\mu_{\text{p/e}} \gtrsim 10$, see Falcke & Biermann 1995), something which might occur naturally if the jet particles originate in an ADAF-like accretion flow.

5.2. The Jet Model and Unification

The result that all six LLAGNs are predicted to have small inclination angles by the jet model is somewhat puzzling. The six LLAGNs in this sample were selected from HU01 on the basis of their VLA spectral indices and 5 GHz flux densities. They are not extreme in flux density or luminosity, as $\sim 1/4$ of the HU01 sample have larger 5 GHz flux densities, and about $1/3$ of the sample have greater 5 GHz radio powers (see UH01a). The radio power of the Palomar Seyfert galaxies is correlated with the [O III] $\lambda 5007$ luminosity and the

FWHM([N II] $\lambda 6584$) velocity over several orders of magnitude (UH01a, Figures 5 and 6), suggesting that the variation in the apparent radio power is caused primarily by sources having different jet powers, and is not primarily due to an inclination effect. Therefore, we do not expect the six LLAGNs in this study to have any preferential orientation based solely on their apparent radio powers. For randomly oriented jet directions, the probability that any single jet has $i \leq 50^\circ$ to match the $\gamma_e = 300$ model is 0.357, or 2.1×10^{-3} for all six objects to appear in this orientation. These probabilities are further reduced if the NGC 4258 jet model is used.

Other selection effects, however, may break the assumed random distribution. The sources were not selected based on the degree of compactness on VLA scales from HU01, so potentially high i objects were not excluded. The sources *were* selected to have spectral indices $\alpha_{1.4}^5 \geq -0.35$, so a spectral index change with luminosity or orientation could bias our object selection. The FB99 model does predict a spectral index change with inclination angle — but the change is quite small, predicting $\alpha \approx +0.1$ for $i = 25^\circ$, and $\alpha \approx +0.2$ for $50^\circ \lesssim i \lesssim 90^\circ$. At high inclination angles, an absorber located in the plane perpendicular to the jet axis could conceivably obscure the jet close to the black hole, where most of the high-frequency radiation is emitted. This would leave the low-frequency emission produced further away from the black hole, resulting in an overall spectrum with $\alpha < 0$. However, this absorber would have to be optically thick up to at least 43 GHz (J. M. Anderson, et al., in preparation), and would require the jet direction to be independent of AGN type as both Seyfert 1 and Seyfert 2 galaxies have roughly equal numbers of “steep” and “flat” radio spectra (UH01a).

However, for $\alpha > 0$ the Seyfert 1 galaxies in the Ho & Ulvestad (2001) do have slightly higher observed radio powers than the Seyfert 2 galaxies, and hence five Seyfert 1 galaxies and only one Seyfert 2 galaxy were selected by our flux density limits. (More Seyfert 2 galaxies would be included if the limit was decreased to 1 mJy or less.) The FB99 model predicts increased flux-densities for low-inclination sources, so this bias would agree with the model if our sources have low jet-inclination angles. According to the standard Unification Model for AGNs (Antonucci 1993), all AGNs are similar intrinsically, but either show broad emission lines (Type 1) or do not show broad emission lines (Type 2) depending on the inclination angle of the accretion disk. An optically thick torus surrounds the accretion region, and one needs to look down the accretion axis (assumed to be the same as the jet axis) in order to see the broad-line region. According to this model, Type 1 AGNs should have smaller inclination angles than Type 2 AGNs. In their analysis of the Palomar sample, Ho, Filippenko, & Sargent (1997b) found that the ratio of Type 2 to Type 1 Seyfert galaxies was 1.4:1, and the ratio of Type 2 to Type 1 LINER galaxies was 3.3:1. According to the unification model, these ratios correspond to half-opening angles for the torus of 54°

and 40° for Seyfert and LINER tori, respectively. Thus, the unification model predicts small inclination angles for five of our galaxies, in basic agreement with the jet model. Interestingly, Georgantopoulos & Zezas (2003) suggest that NGC 3147, our only Type 2 AGN, is actually a Type 1 Seyfert galaxy which lacks a broad-line region. If true, this would give agreement between unification and the jet model of the radio emission for all of our galaxies.

6. Conclusions

We have performed multifrequency, milliarcsecond-scale radio imaging of six LLAGNs with flat/inverted spectra. All six galaxies have slightly rising spectra throughout the gigahertz range, and are unresolved on scales of 10^3 – 10^4 Schwarzschild radii. The radio powers are higher than predicted by simple ADAF models, but the radio powers and spectra are consistent with dominance by compact radio jets. However, the unresolved nature of the radio emission implies that modified ADAF models including nonthermal electrons are still viable models. Otherwise, jet models require the jets to be seen closer to end-on than to side-on in all six galaxies. This result is consistent with the fact that at least five of the size galaxies are Type 1 galaxies, where unified schemes predict that our viewing angle is within $\sim 45^\circ$ of the jet axis.

We thank Heino Falcke for several useful discussions on jet models and LLAGNs. We would also like to thank Jean Eilek, Sera Markoff, and Feng Yuan for valuable discussions on the physics of accretion and jet models. J.M.A. gratefully acknowledges support from the predoctoral fellowship program from NRAO. The work of L.C.H is funded by the Carnegie Institution of Washington and by NASA grants from the Space Telescope Science Institute (operated by AURA, Inc., under NASA contract NAS5-26555). This research has made use of the SIMBAD database, operated at CDS, Strasbourg, France, and NASA’s Astrophysics Data System.

REFERENCES

Antonucci, R. 1993, *ARA&A*, 31, 473
Barth, A. J., Ho, L. C., & Sargent, W. L. W. 2002, *AJ*, 124, 2607
Beasley, A. J., & Conway, J. E. 1995, in *ASP Conf. Ser.* 82: Very Long Baseline Interferometry and the VLBA, 328

Blandford, R. D., & Begelman, M. C. 1999, MNRAS, 303, L1

Blandford, R. D., & Königl, A. 1979, ApJ, 232, 34

Falcke, H. 1996, ApJ, 464, L67

Falcke, H., & Biermann, P. L. 1995, A&A, 293, 665

—. 1999, A&A, 342, 49, (FB99)

Falcke, H., Goss, W. M., Matsuo, H., Teuben, P., Zhao, J., & Zylka, R. 1998, ApJ, 499, 731

Falcke, H., & Markoff, S. 2000, A&A, 362, 113

Falcke, H., Nagar, N. M., Wilson, A. S., & Ulvestad, J. S. 2000, ApJ, 542, 197

Ferrarese, L., & Merritt, D. 2000, ApJ, 539, L9

Filho, M. E., Barthel, P. D., & Ho, L. C. 2000, ApJS, 129, 93

—. 2002, ApJS, 142, 223

Gebhardt, K., et al. 2000, ApJ, 539, L13

Georgantopoulos, I., & Zezas, A. 2003, ApJ, in press (astro-ph/0305488)

Ghez, A. M., et al. 2003, ApJ, 586, L127

Herrnstein, J. R., Greenhill, L. J., Moran, J. M., Diamond, P. J., Inoue, M., Nakai, N., & Miyoshi, M. 1998, ApJ, 497, L69+

Ho, L. C. 2002, ApJ, 564, 120

Ho, L. C., Filippenko, A. V., & Sargent, W. L. W. 1997a, ApJS, 112, 315

—. 1997b, ApJ, 487, 568

Ho, L. C., & Ulvestad, J. S. 2001, ApJS, 133, 77, (HU01)

Jiménez-Benito, L., Díaz, A. I., Terlevich, R., & Terlevich, E. 2000, MNRAS, 317, 907

Mahadevan, R. 1997, ApJ, 477, 585, (M97)

Manmoto, T., Mineshige, S., & Kusunose, M. 1997, ApJ, 489, 791

McElroy, D. B. 1995, ApJS, 100, 105

Nagar, N. M., Falcke, H., Wilson, A. S., & Ho, L. C. 2000, *ApJ*, 542, 186

Nagar, N. M., Falcke, H., Wilson, A. S., & Ulvestad, J. S. 2002, *A&A*, 392, 53

Napier, P. J., Bagri, D. S., Clark, B. G., Rogers, A. E. E., Romney, J. D., Thompson, A. R., & Walker, R. C. 1993, *Proc. IEEE*, 82, 658

Narayan, R., Mahadevan, R., Grindlay, J. E., Popham, R. G., & Gammie, C. 1998a, *ApJ*, 492, 554

Narayan, R., Mahadevan, R., & Quataert, E. 1998b, in *Theory of Black Hole Accretion Disks*, 148

Narayan, R., & Yi, I. 1994, *ApJ*, 428, L13

—. 1995, *ApJ*, 452, 710

Narayan, R., Yi, I., & Mahadevan, R. 1995, *Nature*, 374, 623

Prugniel, P., et al. 2001, in *Mining the Sky*, 683

Schödel, R., Genzel, R., Ott, T., Eckart, A., Mouawad, N., & Alexander, T. 2003, *ApJ*, in press (astro-ph/0306214)

Solanes, J. M., Sanchis, T., Salvador-Solé, E., Giovanelli, R., & Haynes, M. P. 2002, *AJ*, 124, 2440

Tonry, J. L., Dressler, A., Blakeslee, J. P., Ajhar, E. A., Fletcher, A. B., Luppino, G. A., Metzger, M. R., & Moore, C. B. 2001, *ApJ*, 546, 681

Tremaine, S., et al. 2002, *ApJ*, 574, 740

Tully, R. B. 1988, *Nearby galaxies catalog* (Cambridge: Cambridge University Press)

Ulvestad, J. S., & Ho, L. C. 2001a, *ApJ*, 558, 561, (UH01a)

—. 2001b, *ApJ*, 562, L133, (UH01b)

Ulvestad, J. S., & Wilson, A. S. 1989, *ApJ*, 343, 659

Walker, C., & Chatterjee, S. 1999, *Ionospheric Corrections Using GPS Based Models*, VLBA Scientific Memo 23, NRAO

Whitmore, B. C., McElroy, D. B., & Tonry, J. L. 1985, *ApJS*, 59, 1

Yuan, F., Markoff, S., & Falcke, H. 2002a, A&A, 383, 854

Yuan, F., Markoff, S., Falcke, H., & Biermann, P. L. 2002b, A&A, 391, 139

Yuan, F., Quataert, E., & Narayan, R. 2003, ApJ, in press (astro-ph/0304125)

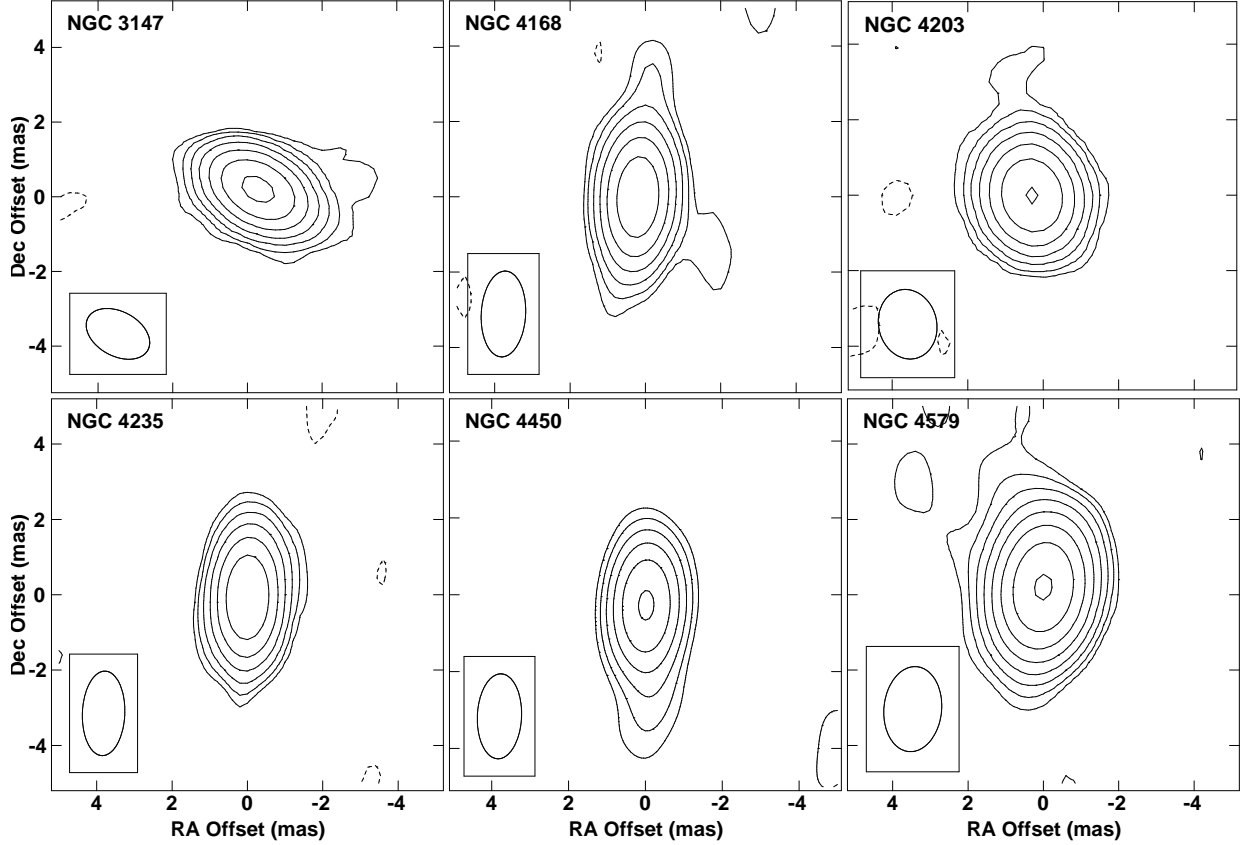


Fig. 1.— The 8.4 GHz VLBA images of the six LLAGNs are shown as contour plots. All images are 10.2 mas on a side, with contour intervals increasing by factors of 2 starting from two times the rms noise level in each image ($54, 44, 63, 47, 66$, and $59 \mu\text{Jy beam}^{-1}$, for NGC 3147, NGC 4168, NGC 4203, NGC 4235, NGC 4450, and NGC 4579, respectively). Negative contours are indicated by dashed lines. The restoring beam for each image is shown in the lower left-hand corner.

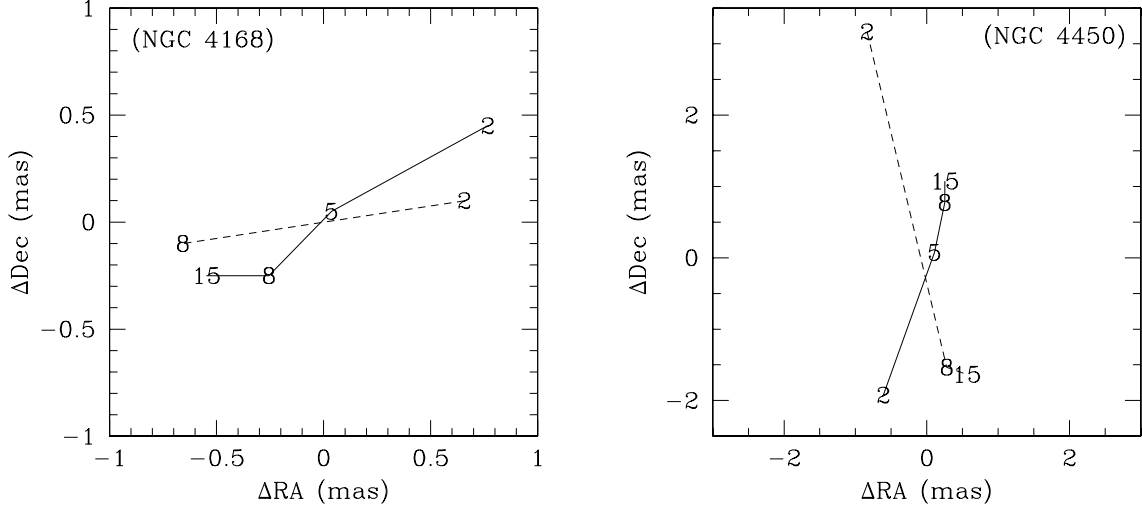


Fig. 2.— Core position is shown as a function of frequency for two target galaxies and their check sources. NGC 4168 (red) is connected by solid lines and its check source (blue) by dashed lines. NGC 4450 (red) is shown with solid lines and its check source (blue) by dashed lines. Numerals are used to indicate the observing frequency (the check sources were not observed at all frequencies). The measured positions have been offset by a constant arbitrary amount for each source. The shift decreases in angular size with increasing frequency. Note that both NGC 4168 and its check source are east-northeast of their phase calibrator, while NGC 4450 is southwest, and its check source northwest of their phase calibrator. The angular separations between the phase calibrator and sources are about twice as large for NGC 4450, probably leading to a larger ionospheric position shift. (See also Tables 1 and 2.)

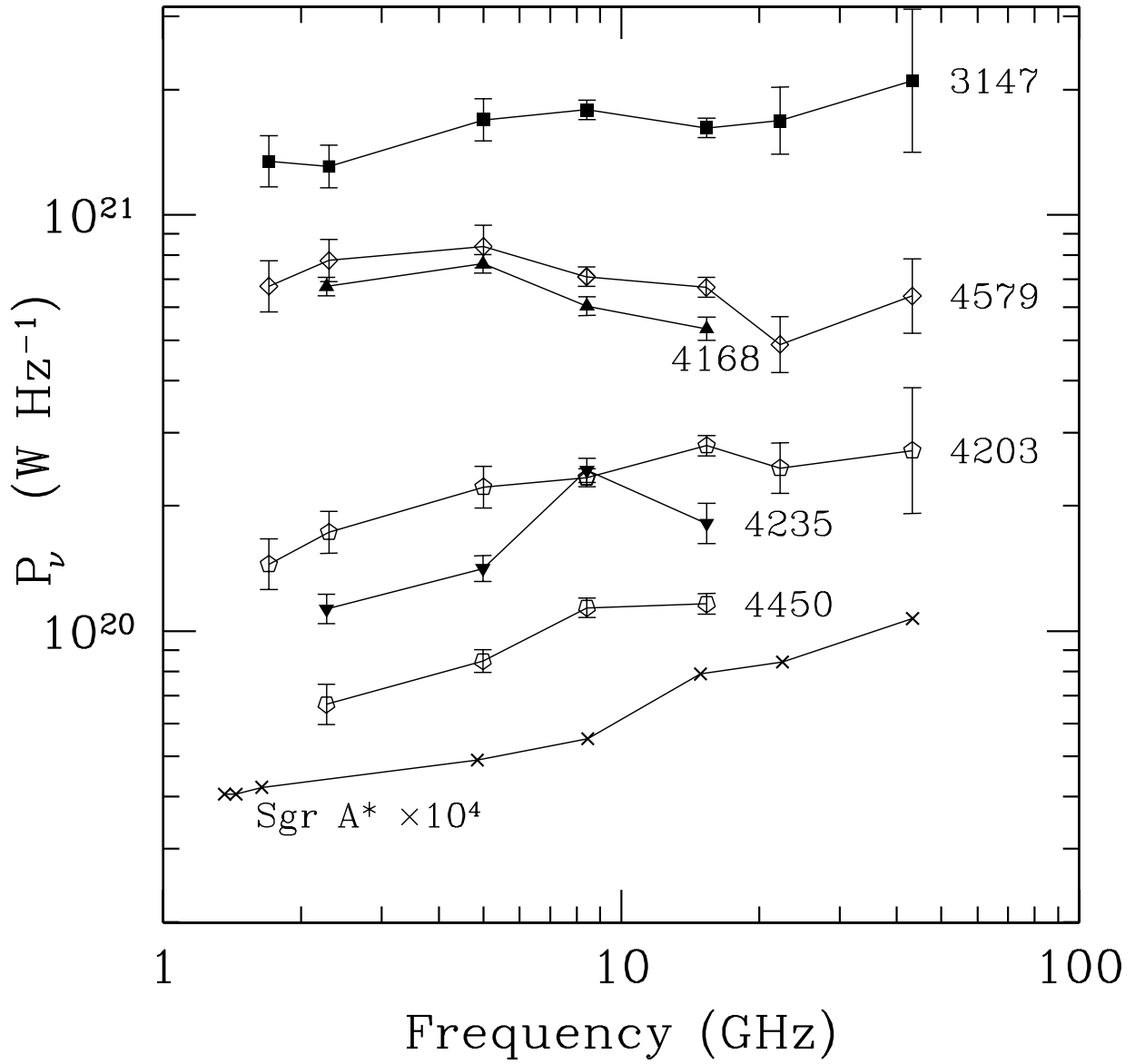


Fig. 3.— The radio powers and uncertainties of the target galaxy cores are shown as a function of frequency, assuming isotropic radiation. For comparison, the spectrum of Sgr A* is shown multiplied by 10^4 (Falcke et al. 1998).

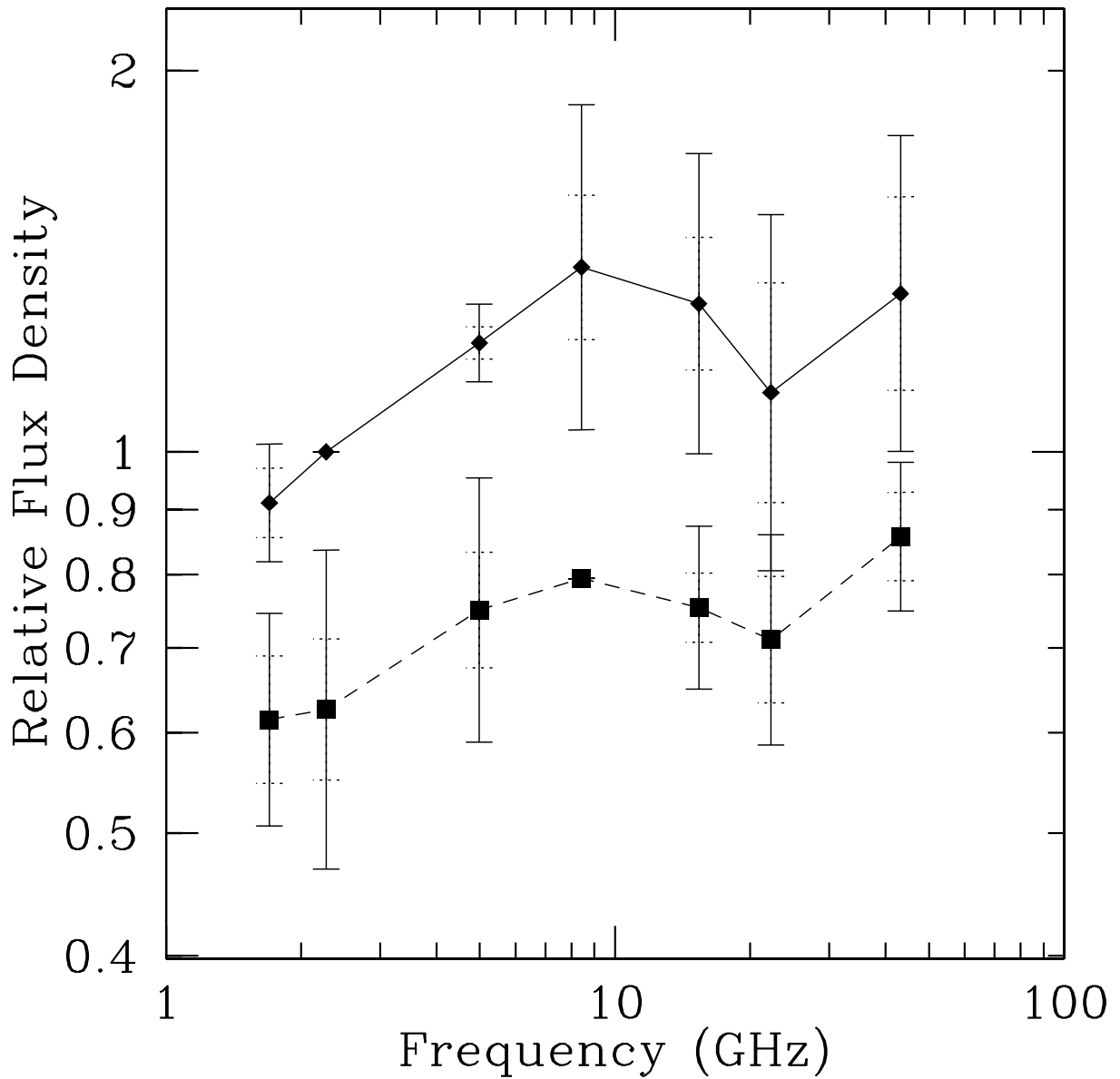


Fig. 4.— Mean spectral energy distributions of the 6 LLAGNs are shown. Data points connected by the solid line were made after normalizing the spectra to unity at 2.3 GHz. The data points connected by the dashed line were first normalized to unity at 8.4 GHz before averaging. These data points have been shifted downward in the figure by 0.1 dex for clarity. Solid error bars show the rms scatter about the mean at each frequency, while the dotted error bars closer in represent the statistical uncertainty in the mean.

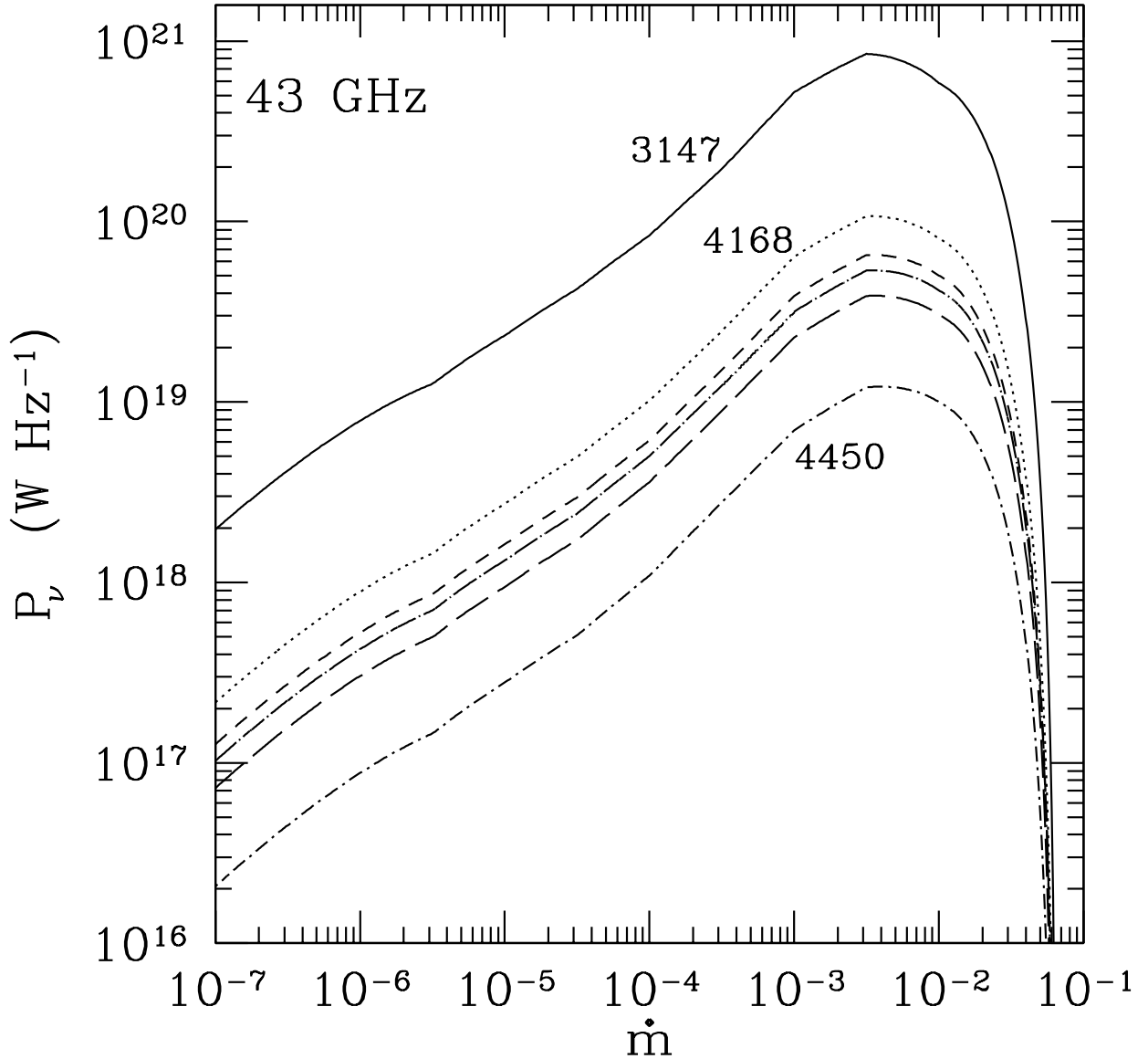


Fig. 5.— The 43 GHz radio power derived from Mahadevan (1997) is shown as a function of the scaled accretion rate for the six LLAGNs in this paper. The emission is low for small \dot{m} as there are few particles to radiate. For large \dot{m} , the particle density becomes high enough that cooling is important, and the electron temperature decreases to a point where synchrotron emission is not produced. NGC 3147 (solid, red), with the highest black hole mass of the sample, has the correspondingly greatest emission for a given \dot{m} . For clarity, NGC 4203 (dashed, blue), NGC 4235 (long dashed, magenta), and NGC 4579 (long-dash

dot, black) are not labeled on the plot.

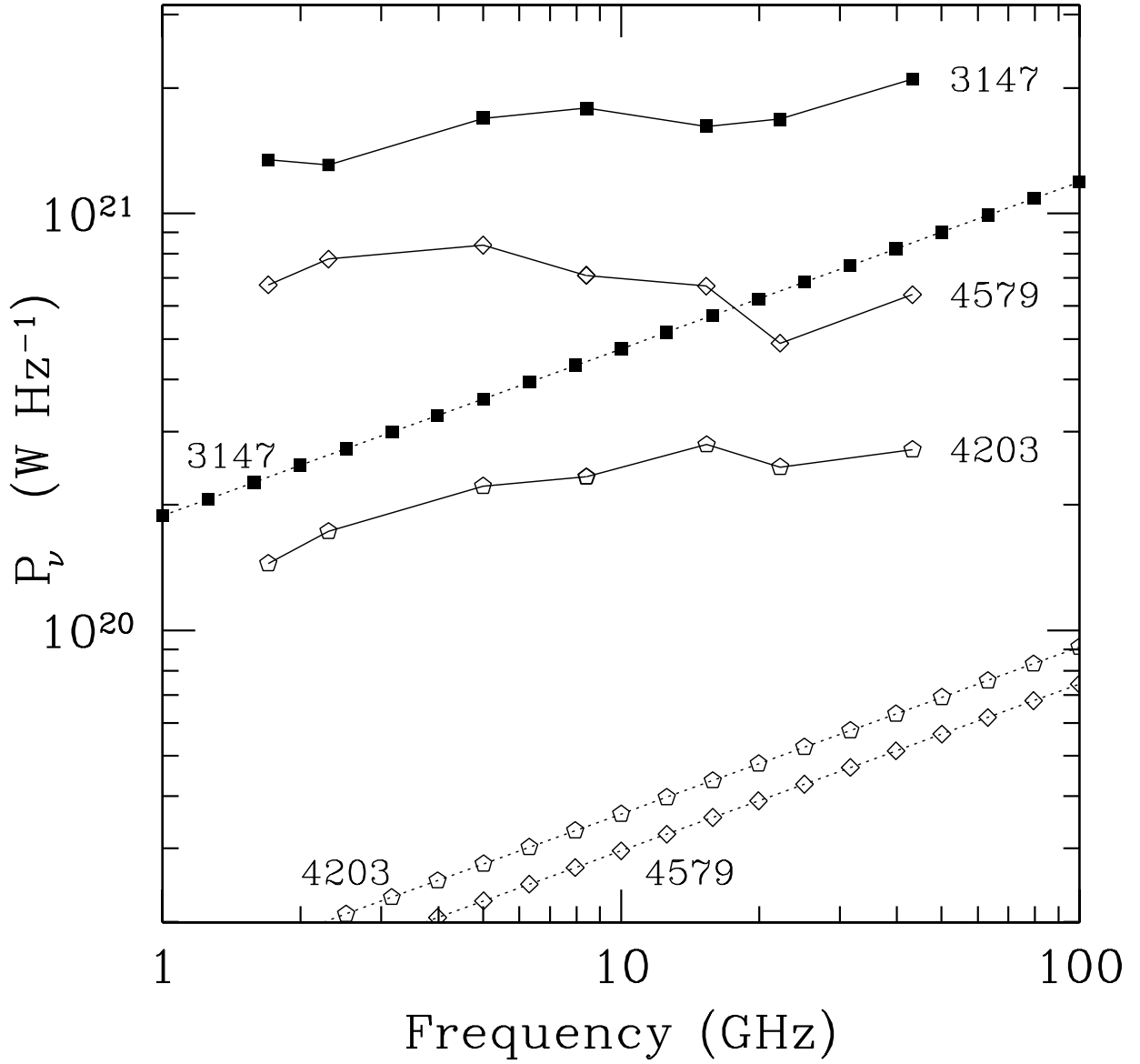


Fig. 6.— The maximum radio power from M97 equation 25 is shown as a function of frequency for three LLAGNs in this sample. The spectrum is calculated for $\dot{m} \approx 10^{-2.5}$, which gives the maximum radio output in the M97 approximation scheme (see also Figure 5). The ADAF models are the regularly spaced points with slope +0.4 and are labeled at the right with their corresponding galaxy. For comparison, the *observed* radio spectra from Figure 3 are also shown. Most of the ADAF models fall a factor of ~ 10 or more below the observations, except for NGC 3147, which is a factor of 2.5 below the 43 GHz observation.

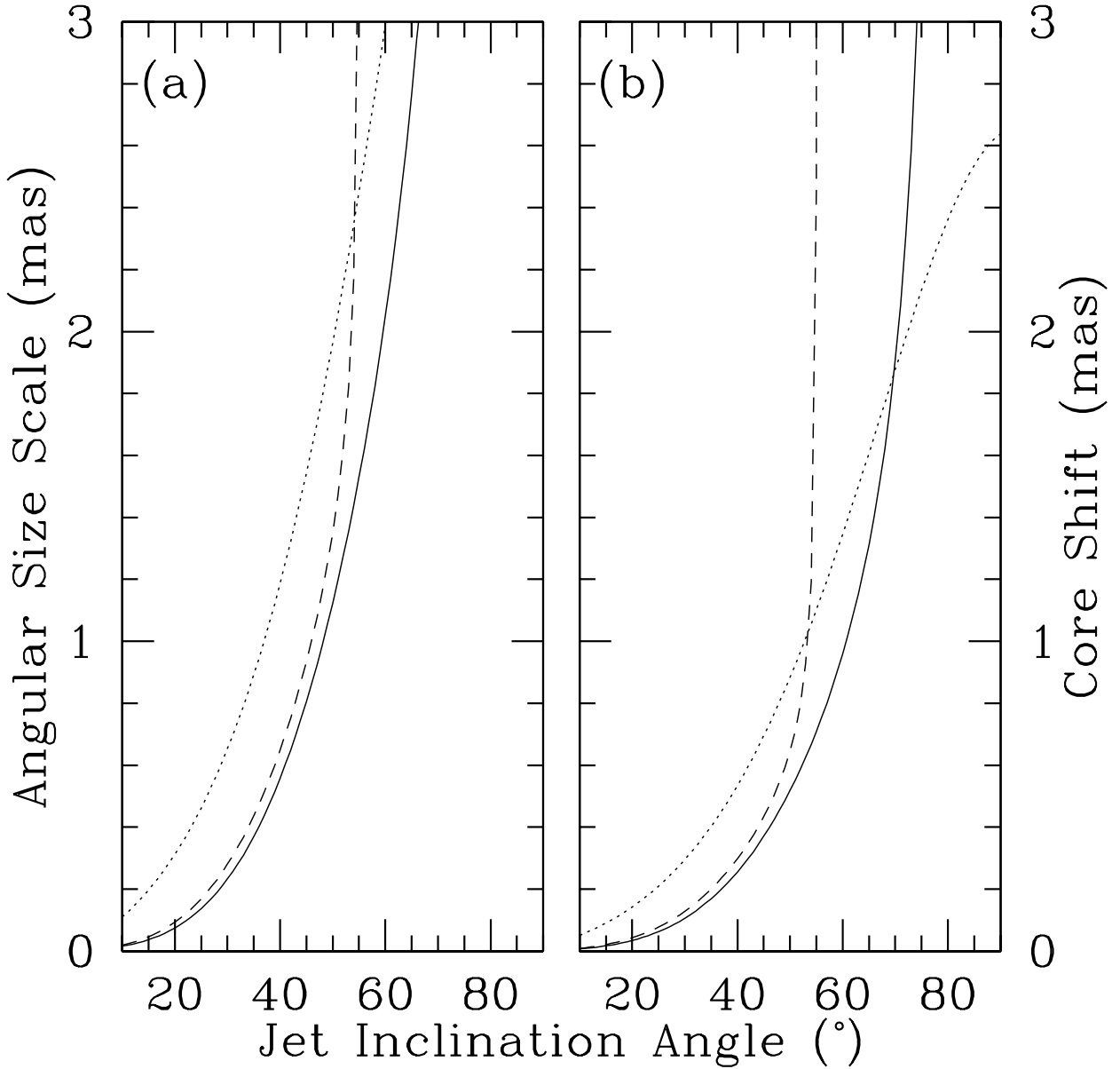


Fig. 7.— The angular size scale at 8.4 GHz ($\Phi_{8.4}$, panel *a*) and core shift ($\Phi_{8.4} - \Phi_{15}$, panel *b*) in milliarcseconds are shown as a function of jet inclination angle for three jet models of NGC 4579. The solid (green) lines correspond to the $\gamma_e = 300$ model; the dotted (red) lines correspond to model parameters similar to NGC 4258 ($\gamma_e = 630$); and the dashed (blue) lines correspond to the $\gamma_e = 250$ model.

Table 1. VLBA Observation Details

Galaxy (1)	UT Date (2)	Frequencies (GHz) (3)	Phase Calibrator (4)	Offset (°) (5)	Check (°) (6)
NGC 3147	2002 Jun 21	8.42, 15.37, 22.23, 43.22	J1048+7143	2.89	3.22
NGC 4168	2002 Jul 30	2.27, 4.99, 8.42, 15.37	J1207+1211	1.60	1.80
NGC 4203	2002 May 11	8.42, 15.37, 22.23, 43.22	J1220+3431	1.69	0.91
NGC 4235	2002 Aug 03	2.27, 4.99, 8.42, 15.37	J1214+0829	1.40	2.76
NGC 4450	2002 Aug 27	2.27, 4.99, 8.42, 15.37	J1237+1924	3.18	3.57
NGC 4579	2002 Jun 02	8.42, 15.37, 22.23, 43.22	J1230+1223	1.78	5.87

Note. — Column (1): Galaxy name. Col. (2): UT observing date. Col. (3): Centers of observed frequencies. Col. (4): Calibration source for phase referencing. Col. (5): Angular separation between sources (1) and (4). Col. (6): Angular separation between the phase calibrator and the check source.

Table 2. Galaxy Attributes

Galaxy (1)	α (J2000) (2)	δ (J2000) (3)	rms (mas) (4)	D (Mpc) (5)	Ref. (6)	σ (km s $^{-1}$) (7)	Ref. (8)	M_{BH} (M $_{\odot}$) (9)	Class (10)
NGC 3147	10 16 53.6503	+73 24 02.696	2.3	40.9	1	269	2	4.4×10^8	S2
NGC 4168	12 12 17.2685	+13 12 18.701	1.4	30.9	3	186	4	1.0×10^8	S1.9:
NGC 4203	12 15 05.0554	+33 11 50.382	1.6	15.1	3	170	5	7.0×10^7	L1.9
NGC 4235	12 17 09.8818	+07 11 29.670	1.5	18.0	6	155	7	4.8×10^7	S1.2
NGC 4450	12 28 29.5908	+17 05 05.972	2.1	14.1	6	126	8	2.1×10^7	L1.9
NGC 4579	12 37 43.5223	+11 49 05.488	2.0	19.1	6	164	4	6.1×10^7	S1.9/L1.9

Note. — Column (1) gives the galaxy name, while Columns (2) and (3) give 8.4 GHz VLBA position of the nuclear core (units of right ascension are hours, minutes, and seconds, and units of declination are degrees, arcminutes, and arcseconds). Column (4) shows the estimated positional uncertainty in each coordinate, including uncertainty in the phase calibrator position, imaging noise, and residual phase errors. Columns (5) and (6) give the adopted distance to the galaxy and a reference for that distance, while Columns (7) and (8) give the adopted velocity dispersion and reference. The resulting mass estimate of the black hole using Tremaine et al. (2002) is shown in Column (9). Column (10) gives the AGN classification according to Ho et al. (1997a), with S representing Seyfert galaxies and L representing LINERs.

References. — 1. Tully 1988, 2. Whitmore, McElroy, & Tonry 1985, 3. Tonry et al. 2001, 4. HyperLeda database (see Prugniel et al. 2001), 5. Barth, Ho, & Sargent 2002, 6. Solanes et al. 2002, 7. Jiménez-Benito et al. 2000, 8. McElroy 1995.

Table 3. VLBA Flux Density Measurements

Galaxy	$S_{1.7}$ (mJy)	$S_{2.3}$ (mJy)	$S_{5.0}$ (mJy)	$S_{8.4}$ (mJy)	$S_{15.4}$ (mJy)	$S_{22.2}$ (mJy)	$S_{43.2}$ (mJy)
(1)	(2)	(3)	(4)	(5)	(6)	(7)	(8)
NGC 3147	6.7 ± 1.0	6.5 ± 0.8	8.4 ± 1.0	8.9 ± 0.5	8.1 ± 0.4	8.4 ± 1.7	10.5 ± 5.1
NGC 4168	...	5.9 ± 0.3	6.7 ± 0.4	5.3 ± 0.3	4.7 ± 0.3
NGC 4203	5.3 ± 0.8	6.3 ± 0.8	8.1 ± 1.0	8.5 ± 0.4	10.2 ± 0.6	9.0 ± 1.3	9.9 ± 4.1
NGC 4235	...	2.9 ± 0.3	3.7 ± 0.3	6.3 ± 0.4	4.7 ± 0.6
NGC 4450	...	2.8 ± 0.3	3.6 ± 0.2	4.8 ± 0.3	4.9 ± 0.3
NGC 4579	15.4 ± 2.3	17.7 ± 2.2	19.2 ± 2.4	16.2 ± 0.9	15.3 ± 0.9	11.1 ± 1.9	14.6 ± 3.3

Note. — Column (1) gives the galaxy name. Columns (2)–(8) give the integrated flux density (S_{ν}) and uncertainty for measurements at 1.7, 2.3, 5.0, 8.4, 15.4, 22.2, and 43.2 GHz. Data values for NGC 3147, NGC 4203, and NGC 4579 at 1.7, 2.3, and 5.0 GHz from UH01b have been scaled by multiplication to match the more recent 8.4 GHz flux densities.

Table 4. 8.4 GHz Size Information

Galaxy	Beam (mas)	$\theta_{3\sigma}$ (mas)	T_b (K)	R (R_S)	Φ_{60} (mas)	$i_{\Phi,\max}$ ($^\circ$)	$i_{\Delta\Phi,\max}$ ($^\circ$)
(1)	(2)	(3)	(4)	(5)	(6)	(7)	(8)
NGC 3147	1.82×1.19	0.70	$> 3.1 \times 10^8$	< 1 600	1.6	47	46
NGC 4168	2.28×1.18	0.77	$> 1.5 \times 10^8$	< 6 000	1.2	53	49
NGC 4203	1.86×1.54	0.59	$> 4.2 \times 10^8$	< 3 200	1.5	44	47
NGC 4235	2.24×1.13	0.64	$> 2.7 \times 10^8$	< 6 000	1.3	48	46
NGC 4450	2.21×1.15	0.83	$> 1.2 \times 10^8$	< 14 000	1.2	54	50
NGC 4579	2.26×1.53	0.54	$> 9.6 \times 10^8$	< 4 300	2.0	40	42

Note. — Column (2) gives the size of the restoring beam in milliarcseconds. Column (3) gives the 3σ upper limit to the deconvolved core size along the major axis. Column (4) gives the corresponding lower limit to the brightness temperature of the unresolved core. Column (5) gives the corresponding upper limit to the *radius* of the unresolved core in Schwarzschild radii. Column (6) gives the characteristic scale size of the 8.4 GHz emission for the $\gamma_e = 300$ jet model from FB99 for an inclination angle of 60° . Column (7) gives the maximum inclination angle for the characteristic size scale to remain less than $\theta_{3\sigma}$ at 8.4 GHz, and Column (8) gives the maximum inclination angle which results in an 8.4 to 15 GHz core shift of less than 0.3 mas for the same model. For a jet with NGC 4258 model parameters (FB99), the sizes at $i = 60^\circ$ are about 60% *larger*, and the maximum inclination angles allowed by the size upper limits are about 13% *smaller* than the values in columns (7) and (8).

Table 5. VLBA Spectral Indices

Galaxy	$\alpha_{2.3}^{5.0}$	$\alpha_{8.4}^{15}$
(1)	(2)	(3)
NGC 3147	$+0.33 \pm 0.09$	-0.16 ± 0.13
NGC 4168	$+0.16 \pm 0.09$	-0.21 ± 0.14
NGC 4203	$+0.32 \pm 0.09$	$+0.30 \pm 0.13$
NGC 4235	$+0.29 \pm 0.14$	-0.49 ± 0.23
NGC 4450	$+0.30 \pm 0.17$	$+0.04 \pm 0.13$
NGC 4579	$+0.10 \pm 0.09$	-0.10 ± 0.13

Note. — Radio spectral indices measured with the VLBA are shown for individual galaxies. Column (2) shows the spectral index from 2.3 to 5.0 GHz, and Column (3) shows the spectral index from 8.4 to 15 GHz. ($S_\nu \propto \nu^{+\alpha}$.)